

Intertwined van-Hove Singularities as a Mechanism for Loop Current Order in Kagome Metals

Heqiu Li,¹ Yong Baek Kim,^{1,2,*} and Hae-Young Kee^{1,3,†}

¹Department of Physics, University of Toronto, Toronto, Ontario M5S 1A7, Canada

²School of Physics, Korea Institute for Advanced Study, Seoul 02455, Korea

³Canadian Institute for Advanced Research, CIFAR Program in Quantum Materials, Toronto, Ontario M5G 1M1, Canada

(Dated: April 4, 2024)

Recent experiments on kagome metals AV_3Sb_5 ($A=Cs, Rb, K$) indicated spontaneous time-reversal symmetry breaking in the charge density wave state in the absence of static magnetization. The loop current order (LCO) is proposed as its cause, but a microscopic model explaining the emergence of LCO through electronic correlations has not been firmly established. We show that the coupling between van-Hove singularities (vHS) with distinct mirror symmetries is a key ingredient to generate LCO ground state. By constructing an effective model, we find that when multiple vHS with opposite mirror eigenvalues are close in energy, the nearest-neighbor electron repulsion favors a ground state with coexisting LCO and charge bond order. It is then demonstrated that this mechanism applies to the kagome metals AV_3Sb_5 . Our findings provide an intriguing mechanism of LCO and pave the way for a deeper understanding of complex quantum phenomena in kagome systems.

Introduction— The vanadium-based kagome metals AV_3Sb_5 ($A=Cs, Rb, K$) have generated considerable interest due to the discovery of exotic phases in this family of materials [1–28]. Superconductivity in these materials emerges at $T_c \sim 0.9 - 2.8K$ [29–32], with magnetoresistance measurements indicating the possibility of novel superconductivity with charge $4e$ and $6e$ flux quantization [33]. Additionally, a 2×2 charge density wave (CDW) is detected below $T_{CDW} \sim 80 - 100K$ [29, 34–38] with scanning tunneling microscopy, emphasizing the important role of vHS at M point of the Brillouin zone. Intriguingly, these materials exhibit spontaneous time-reversal symmetry breaking (TRSB) after the CDW transition, evidenced through techniques such as muon spin relaxation and scanning tunneling microscope [12, 35, 39] in the CDW phase without evidence of static magnetic order [30, 34, 40]. These observations indicate an unconventional CDW order in AV_3Sb_5 .

The observation of TRSB without static magnetic order leads to the hypothesis of loop current order (LCO) [12, 41–43], but the mechanism to generate LCO remains unclear. Enormous experimental and theoretical efforts are devoted to determine the properties of CDW in this kagome system [9, 13, 20, 36, 42–72]. The simplest way to model the system is through a three-band model obtained by assigning a single orbital to each site. When the chemical potential is close to the vHS, incorporating nearest neighbor (NN) electron interactions and electron-phonon coupling leads to a charge bond order (CBO) ground state rather than LCO [20]. Ref.43 shows that LCO can be induced by electron interaction, but this necessitates a substantial next-nearest-neighbor (NNN) interaction, a condition not aligned with realistic scenarios. This poses a critical question: what are the conditions for the emergence of LCO in generic kagome materials?

Noticing the presence of multiple vHS in AV_3Sb_5 , in this paper we demonstrate that when two vHS with *different mirror symmetry eigenvalues* are close to the Fermi level, a simple NN interaction can generate LCO when the coupling between different vHS is taken into account. This ground state has LCO coexisting with CBO, dubbed loop current charge bond

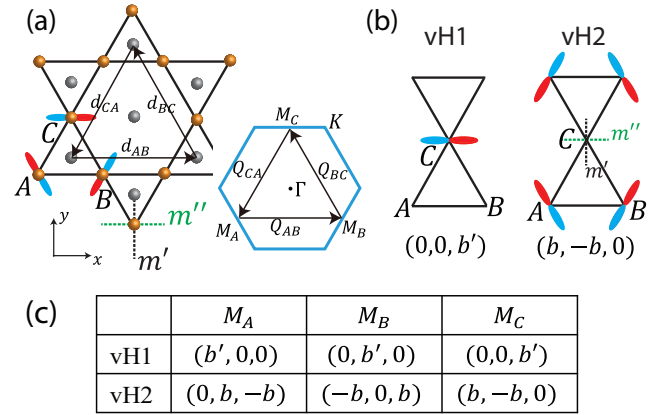


FIG. 1. (a): Kagome plane of AV_3Sb_5 ($A=Cs, Rb, K$). The red (blue) parts denote regions of orbitals with positive (negative) amplitude. The inset shows the Brillouin zone. (b): Real space wave function of vH1 and vH2 at M_C allowed by mirror symmetries. (c): Weight of wave function in (A,B,C) sublattices for vH1 and vH2 at three distinct M points imposed by mirror symmetries, where b and b' are constants.

order (LCBO). We apply this analysis to AV_3Sb_5 by considering a tight binding model with multiple vHS. We find that the ground state of AV_3Sb_5 is LCBO under the conditions described below. This study unveils a mechanism for generating LCO in kagome systems with multiple vHS.

Conditions imposed by mirror symmetries— We first show that mirror symmetries impose important constraints on the wave functions at vHS, which are key ingredients for the emergence of LCBO. Each vHS at momentum M has little group D_{2h} with mutually perpendicular mirror planes m_z, m', m'' , where m_z coincides with kagome plane, m' and m'' are shown in Fig.1(a). Consider two vHS near the Fermi level denoted by vH1 and vH2 at the three distinct momenta M denoted by M_A, M_B, M_C as in Fig.1(a). We show that mirror symmetries will constrain the wave function of vH1 and vH2 at three distinct M points to take the form of Fig.1(c) as long as the

following conditions are satisfied: (1) The wave functions of vH1 and vH2 have opposite eigenvalues under m' and same eigenvalues under m'' . (2) vH1 and vH2 consist of the same type of orbital at the kagome sites.

To demonstrate this conclusion explicitly, we consider two vHS made of the colored orbitals in Fig.1(a), and let the wave function at vH1 (vH2) be odd (even) under m' . Let us inspect the form of symmetry-allowed wave function at momentum M_C as shown in Fig.1(b). In this case, m' coincides with m_x which maps sublattice A and B to each other and maps sublattice C to itself. Because the wave function of vH2 is even under m' and the orbital at sublattice C is odd under m' , the weight of wave function must vanish at m' -invariant sublattice C. Furthermore, wave function components of vH2 at sublattice A and B must have opposite signs to make the wave function even under m' . Therefore, the wave function of vH2 at momentum M_C must take the form $(b, -b, 0)$ at A,B,C sublattices respectively, where b is a constant. A similar analysis can be applied to vH1, which gives the form of $(0, 0, b')$ instead, where b' is another constant. Finally, the threefold rotation symmetry leads to the wave function structure at the three distinct M points given in Fig.1(c). Similarly, this wave function structure can also be obtained for orbitals with other mirror eigenvalues, as shown in Sec.I of the supplementary material (SM) [73].

Effective model for coupled vHS— We construct an effective model that describes the coupling between different vHS. The order parameter for a complex CDW with 2×2 periodicity is written as:

$$\Delta_{\alpha\beta} = \frac{V}{2N_c} \sum_{\mathbf{R}} \left(\langle c_{\mathbf{R},\alpha}^\dagger c_{\mathbf{R},\beta} \rangle - \langle c_{\mathbf{R},\alpha}^\dagger c_{\mathbf{R}-\mathbf{d}_{\alpha\beta},\beta} \rangle \right) \cos(\mathbf{Q}_{\alpha\beta} \cdot \mathbf{R}), \quad (1)$$

Here \mathbf{R} labels unit cells, V is the NN interaction strength, N_c is the number of unit cells, $\alpha, \beta = A, B, C$ denote the kagome sublattices and $\mathbf{Q}_{\alpha\beta}$ connects different momenta M as in Fig.1(a). In phases that preserve threefold rotation symmetry, the order parameters satisfy $\Delta_{AB} = \Delta_{BC} = \Delta_{CA} \equiv \Delta$. The real part of Δ represents CBO, the imaginary part represents LCO and a complex value of Δ represents the coexisting phase of LCO and CBO, denoted as LCBO in Fig.2(a). The phase with real $\Delta > 0$ ($\Delta < 0$) is denoted as CBO^+ (CBO^-) as shown in Fig.2(b,c). There are other possible LCO phases distinct from the ones in Fig.2, but those phases have higher free energy as shown in Sec.IV of SM, hence we mainly focus on the phases in Fig.2.

We can construct an effective model on patches near the three M points. This model can effectively capture the coupling between different vHS, which is the dominant contribution leading to the LCBO ground state. The coupling between vHS at different M points is proportional to the order parameter with coupling strength determined by the wave function components at vHS. We choose the basis $u_1(M_A), u_1(M_B), u_1(M_C), u_2(M_A), u_2(M_B), u_2(M_C)$ where u_1, u_2 denotes the wave function for vH1 and vH2 respectively. Let \mathbf{k} denote the small deviation from M with $|\mathbf{k}| < k_{cut}$. Given the form of wave functions in Fig.1(c) and the order

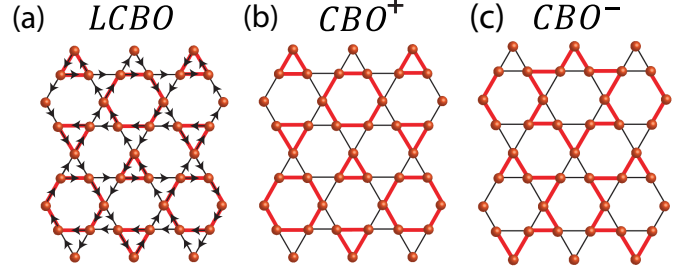


FIG. 2. (a): Coexisting loop current order and charge bond order (LCBO). The red bonds represent modulations of $\langle c_{\mathbf{r}}^\dagger c_{\mathbf{r}'} \rangle$ at NN bonds and the arrows represent current $I \sim \langle ic_{\mathbf{r}}^\dagger c_{\mathbf{r}'} - ic_{\mathbf{r}'}^\dagger c_{\mathbf{r}} \rangle$. (b): Charge bond order with $\Delta > 0$. (c): Charge bond order with $\Delta < 0$.

parameter in Eq.(1), the effective Hamiltonian with leading terms in \mathbf{k} is derived in Sec.II of SM to be:

$$H_{\text{eff}}(\mathbf{k}, \Delta) = \begin{pmatrix} \epsilon_1 & s_1\Delta & s_1\Delta^* & \lambda^*k_1 & 0 & 0 \\ s_1\Delta^* & \epsilon_1 & s_1\Delta & 0 & \lambda^*k_2 & 0 \\ s_1\Delta & s_1\Delta^* & \epsilon_1 & 0 & 0 & \lambda^*k_3 \\ \lambda k_1 & 0 & 0 & \epsilon_2 & s_2\Delta^* & s_2\Delta \\ 0 & \lambda k_2 & 0 & s_2\Delta & \epsilon_2 & s_2\Delta^* \\ 0 & 0 & \lambda k_3 & s_2\Delta^* & s_2\Delta & \epsilon_2 \end{pmatrix}, \quad (2)$$

$$\equiv \begin{pmatrix} P_1 & Q^\dagger \\ Q & P_2 \end{pmatrix}.$$

Here P_1, P_2, Q are 3×3 matrices, $k_1 = -\frac{1}{2}k_x + \frac{\sqrt{3}}{2}k_y, k_2 = -\frac{1}{2}k_x - \frac{\sqrt{3}}{2}k_y, k_3 = k_x$. ϵ_1 and ϵ_2 denote the energies of vH1 and vH2 respectively. The chemical potential μ is set between ϵ_1 and ϵ_2 . Let's first inspect the form of P matrices imposed by symmetries. The matrix P_1 (P_2) describes the effect of CDW order on vH1 (vH2) at momenta M_A, M_B, M_C . The threefold rotation symmetry permutes the three M points, which requires $(P_n)_{12} = (P_n)_{23} = (P_n)_{31}$ for $n = 1, 2$, and whether these matrix elements are related to Δ or Δ^* is determined by the wave function at vHS. The coefficients s_1 and s_2 are determined by wave functions at the vHS, which are found to be $s_1 = -2|b'|^2$ and $s_2 = 2|b|^2$. The relative sign difference in these coefficients comes from the $-b$ term in Fig.1(c) as shown in Sec.III of SM, which is a consequence of the mirror symmetries.

Another important consequence of the mirror symmetries is that they enforce the Q matrix in the off-diagonal block to be a diagonal matrix. With the wave function structure in Fig.1(c), the off-diagonal elements of Q must vanish because they are multiplied by the zeros of wave function components from either vH1 or vH2, as shown in Sec.III of SM. Therefore, only the diagonal terms remain in the Q matrix, which describes the coupling between two vHS at the same M point. These terms are linear in \mathbf{k} because ϵ_1 and ϵ_2 are exact eigenvalues when both \mathbf{k} and Δ are zero, hence at $\mathbf{k} = 0$ the diagonal terms should vanish and the leading order is linear in \mathbf{k} .

Mechanism to generate LCBO— We now discuss the last condition for LCBO to be the ground state of a system described by Eq.(S7). To derive this, we start from the limit

with $\lambda = 0$ and do a perturbation theory on λ . When $\lambda = 0$, $H_{\text{eff}}(\mathbf{k}, \Delta)$ and $H_{\text{eff}}(\mathbf{k}, \Delta e^{\frac{2\pi i}{3}})$ have the same eigenvalues because they are related by a gauge transformation $\mathcal{U} = \text{diag}\{1, \omega, \omega^*, 1, \omega^*, \omega\}$ with $\omega = e^{\frac{2\pi i}{3}}$. Hence when $\lambda = 0$ the free energy F is invariant under $\Delta \rightarrow \Delta e^{\frac{2\pi i}{3}}$, and F has degenerate minima at $\Delta = -|\Delta|$ and $\Delta = |\Delta|e^{\pm \frac{\pi}{3}i}$ corresponding to CBO⁻ and LCBO respectively. The eigenvalues of $H_{\text{eff}} - \mu$ at both minima are the same, which are given by:

$$\begin{aligned} E_1 &= \epsilon_2 - \mu - 4|b|^2|\Delta|, & E_2 &= E_3 = \epsilon_1 - \mu - 2|b'|^2|\Delta|, \\ E_4 &= E_5 = \epsilon_2 - \mu + 2|b|^2|\Delta|, & E_6 &= \epsilon_1 - \mu + 4|b'|^2|\Delta| \end{aligned} \quad (3)$$

When the energy separation between vH1 and vH2 is small, the sign of each eigenvalue is determined by the Δ term, hence the negative eigenvalues are E_1, E_2, E_3 . In the low-temperature limit the sum of them determines the free energy. When λ becomes finite, the degenerate minima of F at $\Delta = -|\Delta|$ and $|\Delta|e^{\pm \frac{\pi}{3}i}$ corresponding to CBO⁻ and LCBO splits. The amount of splitting can be computed by degenerate perturbation theory that captures the evolution of $E_{1\sim 3}$ with λ . Define $\delta\epsilon \equiv \epsilon_2 - \epsilon_1$ as the separation between vH1 and vH2 and denote A as the system area. We find that the difference in free energy density $f = F/A$ between CBO⁻ and LCBO is given by:

$$\begin{aligned} f_{\text{CBO}^-} - f_{\text{LCBO}} &= \\ & \sum_{|\mathbf{k}| \leq k_{\text{cut}}} \frac{-2|\lambda|^2(k_1k_2 + k_2k_3 + k_1k_3)|\Delta|(|b|^2 + |b'|^2)}{A(2|\Delta|(|b|^2 + |b'|^2) + \delta\epsilon)(4|\Delta|(|b|^2 + |b'|^2) - \delta\epsilon)} \\ &= \frac{3}{16\pi} \frac{|\lambda|^2 k_{\text{cut}}^4 |\Delta|(|b|^2 + |b'|^2)}{(2|\Delta|(|b|^2 + |b'|^2) + \delta\epsilon)(4|\Delta|(|b|^2 + |b'|^2) - \delta\epsilon)} > 0. \end{aligned} \quad (4)$$

Eq.(4) shows that for small energy separation $\delta\epsilon < 4(|b|^2 + |b'|^2)|\Delta|$, a finite coupling λ between the two vHS will make LCBO have lower energy and be more favorable than the competing phase CBO⁻. This is the mechanism to generate LCBO in kagome systems.

Importantly, we find that the LCBO phase cannot be described by a small order parameter expansion of the Ginzburg-Landau (GL) theory, hence it is not sensitive to the dispersion near vHS. In Sec.V of SM, we demonstrate that the solution corresponding to LCBO cannot be obtained from GL free energy even if high power terms of Δ are included. We also reiterate that the free energy analysis in Eq.(4) leading to an LCBO ground state is a result of the coupling between two vHS with distinct mirror symmetries.

Application to AV₃Sb₅— We apply the above analysis to AV₃Sb₅ and explicitly construct the effective Hamiltonian H_{eff} . We start from a tight binding model that captures multiple vHS near the Fermi level. The bands close to the Fermi level in AV₃Sb₅ are mainly made of d orbitals at V sites and p orbitals at Sb sites. We consider the tight binding model introduced in Ref. [68]. This model includes three p orbitals at each out-of-plane Sb site and one d orbital at each V site. This d orbital is made of a specific linear combination of d_{xz}, d_{yz} orbitals

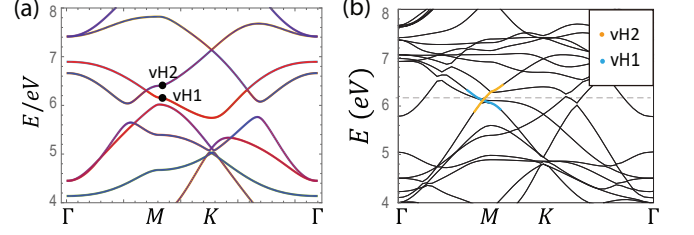


FIG. 3. (a): Band structure of the 9×9 tight-binding model $H_{TB}(\mathbf{k})$ that can reproduce vH1 and vH2. The red color represents the weight of \tilde{d} orbitals in the wave function. (b): Band structure obtained from DFT with vH1 and vH2 highlighted. The figure is adapted from Ref.68.

as indicated by the colored orbitals in Fig.1(a), which is odd (even) under m' (m''), denoted as \tilde{d} orbitals. Hence there are three \tilde{d} orbitals and six p orbitals in each unit cell, leading to a 9-band model $H_{TB}(\mathbf{k})$. The hopping parameters in this model are obtained from DFT band structure [68]. The band structure of $H_{TB}(\mathbf{k})$ is shown in Fig.3(a). Compared with the DFT band structure in Fig.3(b), the 9-band model reproduces two vHS at momentum M denoted by vH1 and vH2. vH1 is odd (even) under m' (m'') and is mainly made of \tilde{d} orbitals. vH2 is even under both m' and m'' and is a superposition of \tilde{d} and p orbitals. Compared with commonly used three-band models that can only describe vH1, this 9-band model can capture both vH1 and vH2, hence it provides a useful platform to study the interplay between different vHS.

Next we consider the NN electron interaction given by

$$H_V = V \sum_{\langle \mathbf{R}\alpha; \mathbf{R}'\beta \rangle} c_{\mathbf{R},\alpha}^\dagger c_{\mathbf{R},\alpha} c_{\mathbf{R}',\beta}^\dagger c_{\mathbf{R}',\beta}, \quad (5)$$

where $\langle \mathbf{R}\alpha; \mathbf{R}'\beta \rangle$ denotes NN bonds. With the order parameter $\Delta_{\alpha\beta}$ defined in Eq.(1), the NN interaction can be mean-field decoupled as [68]:

$$\begin{aligned} H_V^{MF} &= - \sum_{\mathbf{k}} \left(\Delta_{\alpha\beta} (1 - e^{i\mathbf{k} \cdot \mathbf{d}_{\alpha\beta}}) c_{\mathbf{k}-\mathbf{Q}_{\alpha\beta},\beta}^\dagger c_{\mathbf{k},\alpha} + h.c. \right) \\ &+ 2N_c \frac{|\Delta_{\alpha\beta}|^2}{V}, \end{aligned} \quad (6)$$

We can write down a mean field Hamiltonian that includes all bands in Fig.3(a) and the CDW order parameter in Eq.(6) with $\Delta_{AB} = \Delta_{BC} = \Delta_{CA} \equiv \Delta$. To construct the effective patch model H_{eff} , we focus on momenta near the M points and perform a unitary transformation into the band basis in which the basis functions at M points are eigenfunctions of the tight binding model. Then we keep only the matrix elements corresponding to the energies and couplings between vH1 and vH2. This leads to a 6×6 matrix $H_{\text{eff}}(\mathbf{k}, \Delta)$ corresponding to the six patches at vH1 and vH2 near the three M points. By performing a Taylor expansion in \mathbf{k} and keeping leading order terms, we obtain H_{eff} in Eq.(S7) with parameters $\epsilon_1 =$

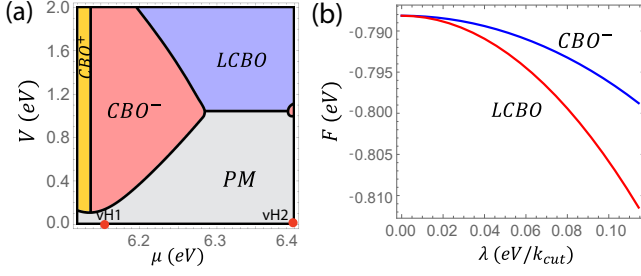


FIG. 4. (a): Phase diagram of H_{eff} at different interaction strength and chemical potential with parameters: $\epsilon_1 = 6.16\text{eV}$, $\epsilon_2 = 6.40\text{eV}$, $b = 0.52$, $b' = 0.96$, $\lambda k_{\text{cut}} = 0.1\text{eV}$ and temperature is 90K. PM refers to the pristine metal without any CDW order. (b): Free energy of LCBO and CBO^- as a function of coupling λ at a fixed interaction strength. It shows LCBO is favored at finite λ .

6.16eV , $\epsilon_2 = 6.40\text{eV}$, $b = 0.52$, $b' = 0.96$, $\lambda = 0.35\text{eV} \cdot a$, where $a = 5.48\text{\AA}$ is the lattice constant. Because the wave functions at both vHS have significant weight on \vec{d} orbitals, the coupling λ between the two vHS receives major contribution from the hopping amplitude t_{dd} between nearest-neighbor \vec{d} orbitals hence λ is generally nonzero. With a finite λ , the above theory for LCBO is applicable to AV_3Sb_5 , indicating that the LCBO phase can be stabilized as the ground state.

Phase diagram of CDW orders—The phase diagram of H_{eff} obtained by minimizing the free energy with respect to Δ at different chemical potential and interaction strength is shown in Fig.4(a). The LCBO phase is more pronounced near vH2 due to the difference in wave function structures at vH1 and vH2. Eq.(4) requires the eigenvalues $E_{1\sim 3}$ be negative and $E_{4\sim 6}$ be positive. Based on Eq.(3), these conditions lead to $4|b'|^2|\Delta| > \delta\epsilon$ when $\mu \sim \epsilon_2$, while when $\mu \sim \epsilon_1$ they lead to $4|b|^2|\Delta| > \delta\epsilon$. Since $|b'| > |b|$ due to the larger weight of \vec{d} orbital at vH1, when $\mu \sim \epsilon_2$ it requires smaller $|\Delta|$ and smaller interaction to realize LCBO. This leads to the smaller critical interaction strength near vH2 as shown in the phase diagram. The competition between CBO^- and LCBO depends on the strength of λ . The free energy of the CBO^- and LCBO phases at $\mu = \epsilon_2$, $V = 1.3\text{eV}$ as a function of coupling strength λ is shown in Fig.4(b). It shows LCBO and CBO^- are degenerate when $\lambda = 0$, and a finite λ makes the free energy of LCBO lower than CBO^- , consistent with Eq.(4).

Effects of the other bands—In AV_3Sb_5 there are other bands near the Fermi level and their effects need to be investigated. For this purpose, we consider an effective patch model obtained by adding one more band below vH1 (denoted as ϵ_3) in Fig.3(a) to H_{eff} , which expands it to a 9×9 matrix near the M points. This model includes vH1, vH2 and ϵ_3 , and its phase diagram is shown in Fig.5(a). Compared with Fig.4(a), which only includes vH1 and vH2, the key variation in Fig.5(a) occurs near vH1, which is close to the additional band at ϵ_3 . However, in regions around vH2 that are more distant from ϵ_3 , the two phase diagrams resemble each other, with LCBO emerging in both scenarios. We further demonstrate that the emergence of LCBO inferred from the patch model remains valid when all

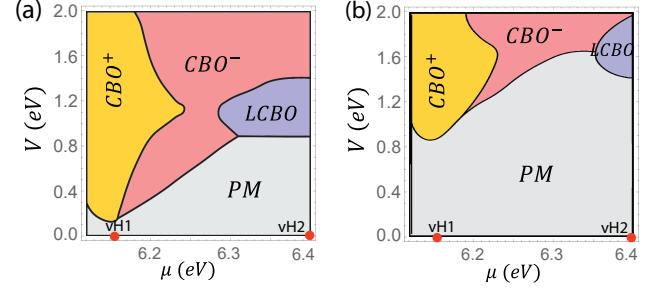


FIG. 5. (a): Phase diagram of the effective patch model obtained by including vH1, vH2 and ϵ_3 . PM refers to the pristine metal without any CDW order. (b): Phase diagram that takes into account all bands in H_{TB} and the momentum summation is over the Brillouin zone. The LCBO phase still exists near vH2.

the bands in the tight-binding model are considered and the momentum cutoff is removed. The phase diagram obtained with all bands in $H_{TB}(\mathbf{k})$ included is shown in Fig.5(b). The real-space configuration of these phases are shown in Fig.2 with the order parameter given in Eq.(1). The summation of momentum in computing the free energy is taken over the whole Brillouin zone. The LCBO phase exists near vH2, whereas near vH1 the ground state is CBO, due to the effect of band structure away from M points and the other bands that are not taken into account in the patch models. This comparison suggests despite the quantitative difference in these phase diagrams, our main finding of LCBO remains valid in the full-band model as long as the chemical potential is near vH2.

Discussion—We provide a mechanism to realize LCBO in kagome systems based on the coupling between multiple vHS with different mirror symmetries. The imaginary part of LCBO breaks time-reversal symmetry, whereas the real part of LCBO can induce lattice distortion with star of David or tri-hexagonal patterns. Experiments on AV_3Sb_5 have observed staggered patterns of lattice distortion among different kagome layers [26]. If the ground state is described by LCBO, we expect the loop current order to be staggered along the c axis as well. Our theory shows LCBO is more favorable when the energy difference $\delta\epsilon$ between vHS is small. Experiments and first-principle computations suggest that pressure can lead to an increase of $\delta\epsilon$ [45, 72], hence we expect LCBO to disappear under high pressure, which is consistent with the disappearance of CDW under high pressure observed in experiments [31, 48, 65, 70]. The phase diagram of AV_3Sb_5 in Fig.5(b) suggests that LCBO emerges when the chemical potential is close to vH2. Thus we predict that electron-doping the material is more likely to induce the LCBO phase. Given the general applicability of our theory to kagome systems having vHS with distinct mirror eigenvalues, we hope this work will inspire further exploration of kagome materials with mirror symmetries.

Acknowledgements—This work is supported by the Natural Sciences and Engineering Research Council of Canada

(NSERC) Discovery Grant No. 2022-04601 and the Center for Quantum Materials at the University of Toronto. H.Y.K acknowledges the support by the Canadian Institute for Advanced Research (CIFAR) and the Canada Research Chairs Program. Y.B.K. is supported by the Simons Fellowship from the Simons Foundation and the Guggenheim Fellowship from the John Simon Guggenheim Memorial Foundation. Computations were performed on the Niagara supercomputer at the SciNet HPC Consortium. SciNet is funded by: the Canada Foundation for Innovation under the auspices of Compute Canada; the Government of Ontario; Ontario Research Fund - Research Excellence; and the University of Toronto.

* ybkim@physics.utoronto.ca

† hykee@physics.utoronto.ca

- [1] Kun Jiang, Tao Wu, Jia-Xin Yin, Zhenyu Wang, M Zahid Hasan, Stephen D Wilson, Xianhui Chen, and Jiangping Hu, “Kagome superconductors AV_3Sb_5 ($A=K, Rb, Cs$),” *National Science Review* (2022), 10.1093/nsr/nwac199, nwac199.
- [2] Shuo-Ying Yang, Yaojia Wang, Brenden R. Ortiz, Defa Liu, Jacob Gayles, Elena Derunova, Rafael Gonzalez-Hernandez, Libor Šmejkal, Yulin Chen, Stuart S. P. Parkin, Stephen D. Wilson, Eric S. Toberer, Tyrel McQueen, and Mazhar N. Ali, “Giant, unconventional anomalous hall effect in the metallic frustrated magnet candidate, kv_3sb_5 ,” *Science Advances* **6**, eabb6003 (2020).
- [3] Titus Neupert, M. Michael Denner, Jia-Xin Yin, Ronny Thomale, and M. Zahid Hasan, “Charge order and superconductivity in kagome materials,” *Nature Physics* **18**, 137–143 (2022).
- [4] Yaojia Wang, Shuoying Yang, Pranava K. Sivakumar, Brenden R. Ortiz, Samuel M. L. Teicher, Heng Wu, Abhay K. Srivastava, Chirag Garg, Defa Liu, Stuart S. P. Parkin, Eric S. Toberer, Tyrel McQueen, Stephen D. Wilson, and Mazhar N. Ali, “Proximity-induced spin-triplet superconductivity and edge supercurrent in the topological kagome metal, $K_{1-x}V_3Sb_5$ ” (2020), [arXiv:2012.05898](https://arxiv.org/abs/2012.05898).
- [5] Yong Hu, Xianxin Wu, Brenden R. Ortiz, Sailong Ju, Xinlong Han, Junzhang Ma, Nicholas C. Plumb, Milan Radovic, Ronny Thomale, Stephen D. Wilson, Andreas P. Schnyder, and Ming Shi, “Rich nature of van hove singularities in kagome superconductor csv_3sb_5 ,” *Nature Communications* **13**, 2220 (2022).
- [6] Yuzki M. Oey, Brenden R. Ortiz, Farnaz Kaboudvand, Jonathan Frassinetti, Erick Garcia, Rong Cong, Samuele Sanna, Vesna F. Mitrović, Ram Seshadri, and Stephen D. Wilson, “Fermi level tuning and double-dome superconductivity in the kagome metal $csv_3sb_{5-x}sn_x$,” *Phys. Rev. Mater.* **6**, L041801 (2022).
- [7] Morten H. Christensen, Turan Birol, Brian M. Andersen, and Rafael M. Fernandes, “Loop currents in av_3sb_5 kagome metals: Multipolar and toroidal magnetic orders,” *Phys. Rev. B* **106**, 144504 (2022).
- [8] C. C. Zhu, X. F. Yang, W. Xia, Q. W. Yin, L. S. Wang, C. C. Zhao, D. Z. Dai, C. P. Tu, B. Q. Song, Z. C. Tao, Z. J. Tu, C. S. Gong, H. C. Lei, Y. F. Guo, and S. Y. Li, “Double-dome superconductivity under pressure in the v -based kagome metals av_3sb_5 ($a = Rb$ and k),” *Phys. Rev. B* **105**, 094507 (2022).
- [9] Q. Stahl, D. Chen, T. Ritschel, C. Shekhar, E. Sadrollahi, M. C. Rahn, O. Ivashko, M. v. Zimmermann, C. Felser, and J. Geck, “Temperature-driven reorganization of electronic order in csv_3sb_5 ,” *Phys. Rev. B* **105**, 195136 (2022).
- [10] Shangfei Wu, Brenden R. Ortiz, Hengxin Tan, Stephen D. Wilson, Binghai Yan, Turan Birol, and Girsh Blumberg, “Charge density wave order in the kagome metal av_3sb_5 ($a = Cs, Rb, K$),” *Phys. Rev. B* **105**, 155106 (2022).
- [11] Mingu Kang, Shiang Fang, Jeong-Kyu Kim, Brenden R. Ortiz, Sae Hee Ryu, Jimin Kim, Jonggyu Yoo, Giorgio Sangiovanni, Domenico Di Sante, Byeong-Gyu Park, Chris Jozwiak, Aaron Bostwick, Eli Rotenberg, Efthimios Kaxiras, Stephen D. Wilson, Jae-Hoon Park, and Riccardo Comin, “Twofold van hove singularity and origin of charge order in topological kagome superconductor csv_3sb_5 ,” *Nature Physics* **18**, 301–308 (2022).
- [12] Yu-Xiao Jiang, Jia-Xin Yin, M. Michael Denner, Nana Shumiya, Brenden R. Ortiz, Gang Xu, Zurab Guguchia, Junyi He, Md Shafayat Hossain, Xiaoxiong Liu, Jacob Ruff, Linus Kautzsch, Songtian S. Zhang, Guoqing Chang, Ilya Belopolski, Qi Zhang, Tyler A. Cochran, Daniel Multer, Maksim Litskevich, Zi-Jia Cheng, Xian P. Yang, Ziqiang Wang, Ronny Thomale, Titus Neupert, Stephen D. Wilson, and M. Zahid Hasan, “Unconventional chiral charge order in kagome superconductor kv_3sb_5 ,” *Nature Materials* **20**, 1353–1357 (2021).
- [13] Haoxiang Li, T. T. Zhang, T. Yilmaz, Y. Y. Pai, C. E. Marvinney, A. Said, Q. W. Yin, C. S. Gong, Z. J. Tu, E. Vescovo, C. S. Nelson, R. G. Moore, S. Murakami, H. C. Lei, H. N. Lee, B. J. Lawrie, and H. Miao, “Observation of unconventional charge density wave without acoustic phonon anomaly in kagome superconductors AV_3Sb_5 ($a = Rb, Cs$),” *Phys. Rev. X* **11**, 031050 (2021).
- [14] Xianxin Wu, Tilman Schwemmer, Tobias Müller, Armando Consiglio, Giorgio Sangiovanni, Domenico Di Sante, Yasir Iqbal, Werner Hanke, Andreas P. Schnyder, M. Michael Denner, Mark H. Fischer, Titus Neupert, and Ronny Thomale, “Nature of unconventional pairing in the kagome superconductors av_3sb_5 ($a = K, Rb, Cs$),” *Phys. Rev. Lett.* **127**, 177001 (2021).
- [15] He Zhao, Hong Li, Brenden R. Ortiz, Samuel M. L. Teicher, Takamori Park, Mengxing Ye, Ziqiang Wang, Leon Balents, Stephen D. Wilson, and Ilija Zeljkovic, “Cascade of correlated electron states in the kagome superconductor csv_3sb_5 ,” *Nature* **599**, 216–221 (2021).
- [16] Hong Li, He Zhao, Brenden R. Ortiz, Takamori Park, Mengxing Ye, Leon Balents, Ziqiang Wang, Stephen D. Wilson, and Ilija Zeljkovic, “Rotation symmetry breaking in the normal state of a kagome superconductor kv_3sb_5 ,” *Nature Physics* **18**, 265–270 (2022).
- [17] Astrid T. Rømer, Shinibali Bhattacharyya, Roser Valentí, Morten H. Christensen, and Brian M. Andersen, “Superconductivity from repulsive interactions on the kagome lattice,” *Phys. Rev. B* **106**, 174514 (2022).
- [18] Thomas Mertz, Paul Wunderlich, Shinibali Bhattacharyya, Francesco Ferrari, and Roser Valentí, “Statistical learning of engineered topological phases in the kagome superlattice of av_3sb_5 ,” *npj Computational Materials* **8**, 66 (2022).
- [19] Andrzej Ptak, Aksel Kobiałka, Małgorzata Sternik, Jan Łażewski, Paweł T. Jochym, Andrzej M. Oleś, and Przemysław Piekarczyk, “Dynamical study of the origin of the charge density wave in av_3sb_5 ($a = K, Rb, Cs$) compounds,” *Phys. Rev. B* **105**, 235134 (2022).
- [20] Francesco Ferrari, Federico Becca, and Roser Valentí, “Charge density waves in kagome-lattice extended hubbard models at the van hove filling,” *Phys. Rev. B* **106**, L081107 (2022).
- [21] Ece Ukyur, Brenden R. Ortiz, Stephen D. Wilson, Martin Dressel, and Alexander A. Tsirlin, “Optical detection of the density-wave instability in the kagome metal kv_3sb_5 ,” *npj Quantum Materials* **7**, 16 (2022).

- [22] Francesco Grandi, Armando Consiglio, Michael A. Sentef, Ronny Thomale, and Dante M. Kennes, “Theory of nematic charge orders in kagome metals,” (2023), [arXiv:2302.01615](https://arxiv.org/abs/2302.01615).
- [23] Yishuai Xu, Zhuoliang Ni, Yizhou Liu, Brenden R. Ortiz, Qinqin Deng, Stephen D. Wilson, Binghai Yan, Leon Balents, and Liang Wu, “Three-state nematicity and magneto-optical kerr effect in the charge density waves in kagome superconductors,” *Nature Physics* **18**, 1470–1475 (2022).
- [24] David R. Saykin, Camron Farhang, Erik D. Kountz, Dong Chen, Brenden R. Ortiz, Chandra Shekhar, Claudia Felser, Stephen D. Wilson, Ronny Thomale, Jing Xia, and Aharon Kapitulnik, “High resolution polar kerr effect studies of csv_3sb_5 : Tests for time-reversal symmetry breaking below the charge-order transition,” *Phys. Rev. Lett.* **131**, 016901 (2023).
- [25] Yajian Hu, Soichiro Yamane, Giordano Mattoni, Kanae Yada, Keito Obata, Yongkai Li, Yugui Yao, Zhiwei Wang, Jingyuan Wang, Camron Farhang, Jing Xia, Yoshiteru Maeno, and Shingo Yonezawa, “Time-reversal symmetry breaking in charge density wave of csv_3sb_5 detected by polar kerr effect,” (2022), [arXiv:2208.08036](https://arxiv.org/abs/2208.08036).
- [26] Mingu Kang, Shiang Fang, Jonggyu Yoo, Brenden R. Ortiz, Yuzki M. Oey, Jonghyeok Choi, Sae Hee Ryu, Jimin Kim, Chris Jozwiak, Aaron Bostwick, Eli Rotenberg, Efthimios Kaxiras, Joseph G. Checkelsky, Stephen D. Wilson, Jae-Hoon Park, and Riccardo Comin, “Charge order landscape and competition with superconductivity in kagome metals,” *Nature Materials* (2022), [10.1038/s41563-022-01375-2](https://doi.org/10.1038/s41563-022-01375-2).
- [27] Jingyuan Wang, Camron Farhang, Brenden R. Ortiz, Stephen D. Wilson, and Jing Xia, “Resolving the discrepancy between moke measurements at 1550-nm wavelength on kagome metal csv_3sb_5 ,” (2023), [arXiv:2301.08853](https://arxiv.org/abs/2301.08853).
- [28] Stephen D. Wilson and Brenden R. Ortiz, “ Av_3sb_5 kagome superconductors: Progress and future directions,” (2023), [arXiv:2311.05946](https://arxiv.org/abs/2311.05946).
- [29] Brenden R. Ortiz, Samuel M. L. Teicher, Yong Hu, Julia L. Zuo, Paul M. Sarte, Emily C. Schueller, A. M. Milinda Abeykoon, Matthew J. Krogstad, Stephan Rosenkranz, Raymond Osborn, Ram Seshadri, Leon Balents, Junfeng He, and Stephen D. Wilson, “ Csv_3sb_5 : A F_2 topological kagome metal with a superconducting ground state,” *Phys. Rev. Lett.* **125**, 247002 (2020).
- [30] Brenden R. Ortiz, Paul M. Sarte, Eric M. Kenney, Michael J. Graf, Samuel M. L. Teicher, Ram Seshadri, and Stephen D. Wilson, “Superconductivity in the F_2 kagome metal kv_3sb_5 ,” *Phys. Rev. Mater.* **5**, 034801 (2021).
- [31] K. Y. Chen, N. N. Wang, Q. W. Yin, Y. H. Gu, K. Jiang, Z. J. Tu, C. S. Gong, Y. Uwatoko, J. P. Sun, H. C. Lei, J. P. Hu, and J.-G. Cheng, “Double superconducting dome and triple enhancement of T_c in the kagome superconductor csv_3sb_5 under high pressure,” *Phys. Rev. Lett.* **126**, 247001 (2021).
- [32] Hui Chen, Haitao Yang, Bin Hu, Zhen Zhao, Jie Yuan, Yuqing Xing, Guojian Qian, Zihao Huang, Geng Li, Yuhan Ye, Sheng Ma, Shunli Ni, Hua Zhang, Qiangwei Yin, Chunsheng Gong, Zhijun Tu, Hechang Lei, Hengxin Tan, Sen Zhou, Chengmin Shen, Xiaoli Dong, Binghai Yan, Ziqiang Wang, and Hong-Jun Gao, “Roton pair density wave in a strong-coupling kagome superconductor,” *Nature* **599**, 222–228 (2021).
- [33] Jun Ge, Pinyuan Wang, Ying Xing, Qiangwei Yin, Hechang Lei, Ziqiang Wang, and Jian Wang, “Discovery of charge-4e and charge-6e superconductivity in kagome superconductor csv_3sb_5 ,” (2022), [arXiv:2201.10352](https://arxiv.org/abs/2201.10352).
- [34] Brenden R. Ortiz, Lídia C. Gomes, Jennifer R. Morey, Michal Winiarski, Mitchell Bordelon, John S. Mangum, Iain W. H. Oswald, Jose A. Rodriguez-Rivera, James R. Neilson, Stephen D. Wilson, Elif Ertekin, Tyrel M. McQueen, and Eric S. Toberer, “New kagome prototype materials: discovery of kv_3sb_5 , rbv_3sb_5 , and csv_3sb_5 ,” *Phys. Rev. Mater.* **3**, 094407 (2019).
- [35] Nana Shumiya, Md. Shafayat Hossain, Jia-Xin Yin, Yu-Xiao Jiang, Brenden R. Ortiz, Hongxiong Liu, Youguo Shi, Qiangwei Yin, Hechang Lei, Songtian S. Zhang, Guoqing Chang, Qi Zhang, Tyler A. Cochran, Daniel Multer, Maksim Litskevich, Zi-Jia Cheng, Xian P. Yang, Zurab Guguchia, Stephen D. Wilson, and M. Zahid Hasan, “Intrinsic nature of chiral charge order in the kagome superconductor Rbv_3sb_5 ,” *Phys. Rev. B* **104**, 035131 (2021).
- [36] Brenden R. Ortiz, Samuel M. L. Teicher, Linus Kautzsch, Paul M. Sarte, Noah Ratcliff, John Harter, Jacob P. C. Ruff, Ram Seshadri, and Stephen D. Wilson, “Fermi surface mapping and the nature of charge-density-wave order in the kagome superconductor csv_3sb_5 ,” *Phys. Rev. X* **11**, 041030 (2021).
- [37] Jian-Guo Si, Wen-Jian Lu, Yu-Ping Sun, Peng-Fei Liu, and Bao-Tian Wang, “Charge density wave and pressure-dependent superconductivity in the kagome metal csv_3sb_5 : A first-principles study,” *Phys. Rev. B* **105**, 024517 (2022).
- [38] DianWu Song, LiXuan Zheng, FangHang Yu, Jian Li, Lin-Peng Nie, Min Shan, Dan Zhao, ShunJiao Li, BaoLei Kang, ZhiMian Wu, YanBing Zhou, KuangLv Sun, Kai Liu, XiGang Luo, ZhenYu Wang, JianJun Ying, XianGang Wan, Tao Wu, and XianHui Chen, “Orbital ordering and fluctuations in a kagome superconductor csv_3sb_5 ,” *Science China Physics, Mechanics & Astronomy* **65**, 247462 (2022).
- [39] C. Mielke, D. Das, J.-X. Yin, H. Liu, R. Gupta, Y.-X. Jiang, M. Medarde, X. Wu, H. C. Lei, J. Chang, Pengcheng Dai, Q. Si, H. Miao, R. Thomale, T. Neupert, Y. Shi, R. Khasanov, M. Z. Hasan, H. Luetkens, and Z. Guguchia, “Time-reversal symmetry-breaking charge order in a kagome superconductor,” *Nature* **602**, 245–250 (2022).
- [40] Eric M Kenney, Brenden R Ortiz, Chennan Wang, Stephen D Wilson, and Michael J Graf, “Absence of local moments in the kagome metal kv_3sb_5 as determined by muon spin spectroscopy,” *Journal of Physics: Condensed Matter* **33**, 235801 (2021).
- [41] Yu-Ping Lin and Rahul M. Nandkishore, “Chiral twist on the high- T_c phase diagram in moiré heterostructures,” *Phys. Rev. B* **100**, 085136 (2019).
- [42] Hyeok-Jun Yang, Hee Seung Kim, Min Yong Jeong, Yong Baek Kim, Myung Joon Han, and SungBin Lee, “Intertwining orbital current order and superconductivity in kagome metal,” (2022), [arXiv:2203.07365](https://arxiv.org/abs/2203.07365).
- [43] Jin-Wei Dong, Ziqiang Wang, and Sen Zhou, “Loop-current charge density wave driven by long-range coulomb repulsion on the kagomé lattice,” *Phys. Rev. B* **107**, 045127 (2023).
- [44] Linpeng Nie, Kuanglv Sun, Wanru Ma, Dianwu Song, Lixuan Zheng, Zuwei Liang, Ping Wu, Fanghang Yu, Jian Li, Min Shan, Dan Zhao, Shunjiao Li, Baolei Kang, Zhimian Wu, Yanbing Zhou, Kai Liu, Ziji Xiang, Jianjun Ying, Zhenyu Wang, Tao Wu, and Xianhui Chen, “Charge-density-wave-driven electronic nematicity in a kagome superconductor,” *Nature* **604**, 59–64 (2022).
- [45] Harrison LaBollita and Antia S. Botana, “Tuning the van hove singularities in av_3sb_5 ($a = \text{K, Rb, Cs}$) via pressure and doping,” *Phys. Rev. B* **104**, 205129 (2021).
- [46] Hengxin Tan, Yizhou Liu, Ziqiang Wang, and Binghai Yan, “Charge density waves and electronic properties of superconducting kagome metals,” *Phys. Rev. Lett.* **127**, 046401 (2021).
- [47] Zuwei Liang, Xingyuan Hou, Fan Zhang, Wanru Ma, Ping Wu, Zongyuan Zhang, Fanghang Yu, J.-J. Ying, Kun Jiang, Lei Shan, Zhenyu Wang, and X.-H. Chen, “Three-dimensional

- charge density wave and surface-dependent vortex-core states in a kagome superconductor csv_3sb_5 ,” *Phys. Rev. X* **11**, 031026 (2021).
- [48] F. H. Yu, D. H. Ma, W. Z. Zhuo, S. Q. Liu, X. K. Wen, B. Lei, J. J. Ying, and X. H. Chen, “Unusual competition of superconductivity and charge-density-wave state in a compressed topological kagome metal,” *Nature Communications* **12**, 3645 (2021).
- [49] Zhicheng Jiang, Haiyang Ma, Wei Xia, Zhengtai Liu, Qian Xiao, Zhonghao Liu, Yichen Yang, Jianyang Ding, Zhe Huang, Jiayu Liu, Yuxi Qiao, Jishan Liu, Yingying Peng, Soohyun Cho, Yanfeng Guo, Jianpeng Liu, and Dawei Shen, “Observation of electronic nematicity driven by the three-dimensional charge density wave in kagome lattice kv_3sb_5 ,” *Nano Letters* **23**, 5625–5633 (2023).
- [50] Ethan T. Ritz, Rafael M. Fernandes, and Turan Birol, “Impact of sb degrees of freedom on the charge density wave phase diagram of the kagome metal csv_3sb_5 ,” *Phys. Rev. B* **107**, 205131 (2023).
- [51] Yong Hu, Xianxin Wu, Brenden R. Ortiz, Xinloong Han, Nicholas C. Plumb, Stephen D. Wilson, Andreas P. Schnyder, and Ming Shi, “Coexistence of trihexagonal and star-of-david pattern in the charge density wave of the kagome superconductor av_3sb_5 ,” *Phys. Rev. B* **106**, L241106 (2022).
- [52] J. Luo, Z. Zhao, Y. Z. Zhou, J. Yang, A. F. Fang, H. T. Yang, H. J. Gao, R. Zhou, and Guo-qing Zheng, “Possible star-of-david pattern charge density wave with additional modulation in the kagome superconductor csv_3sb_5 ,” *npj Quantum Materials* **7**, 30 (2022).
- [53] Chao Mu, Qiangwei Yin, Zhijun Tu, Chunsheng Gong, Ping Zheng, Hechang Lei, Zheng Li, and Jianlin Luo, “Tri-hexagonal charge order in kagome metal csv_3sb_5 revealed by 121sb nuclear quadrupole resonance,” *Chinese Physics B* **31**, 017105 (2022).
- [54] Hailan Luo, Qiang Gao, Hongxiong Liu, Yuhao Gu, Dingsong Wu, Changjiang Yi, Junjie Jia, Shilong Wu, Xiangyu Luo, Yu Xu, Lin Zhao, Qingyan Wang, Hanqing Mao, Guodong Liu, Zhihai Zhu, Youguo Shi, Kun Jiang, Jiangping Hu, Zuyan Xu, and X. J. Zhou, “Electronic nature of charge density wave and electron-phonon coupling in kagome superconductor kv_3sb_5 ,” *Nature Communications* **13**, 273 (2022).
- [55] Takemi Kato, Yongkai Li, Tappei Kawakami, Min Liu, Kosuke Nakayama, Zhiwei Wang, Ayumi Moriya, Kiyohisa Tanaka, Takashi Takahashi, Yugui Yao, and Takafumi Sato, “Three-dimensional energy gap and origin of charge-density wave in kagome superconductor kv_3sb_5 ,” *Communications Materials* **3**, 30 (2022).
- [56] Soohyun Cho, Haiyang Ma, Wei Xia, Yichen Yang, Zhengtai Liu, Zhe Huang, Zhicheng Jiang, Xiangle Lu, Jishan Liu, Zhonghao Liu, Jun Li, Jinghui Wang, Yi Liu, Jinfeng Jia, Yanfeng Guo, Jianpeng Liu, and Dawei Shen, “Emergence of new van hove singularities in the charge density wave state of a topological kagome metal rbv_3sb_5 ,” *Phys. Rev. Lett.* **127**, 236401 (2021).
- [57] M. Michael Denner, Ronny Thomale, and Titus Neupert, “Analysis of charge order in the kagome metal av_3sb_5 ($a = \text{K, Rb, Cs}$),” *Phys. Rev. Lett.* **127**, 217601 (2021).
- [58] Takamori Park, Mengxing Ye, and Leon Balents, “Electronic instabilities of kagome metals: Saddle points and landau theory,” *Phys. Rev. B* **104**, 035142 (2021).
- [59] Yu-Ping Lin and Rahul M. Nandkishore, “Complex charge density waves at van hove singularity on hexagonal lattices: Haldane-model phase diagram and potential realization in the kagome metals av_3sb_5 ($a = \text{k, rb, cs}$),” *Phys. Rev. B* **104**, 045122 (2021).
- [60] Morten H. Christensen, Turan Birol, Brian M. Andersen, and Rafael M. Fernandes, “Theory of the charge density wave in av_3sb_5 kagome metals,” *Phys. Rev. B* **104**, 214513 (2021).
- [61] Min Yong Jeong, Hyeok-Jun Yang, Hee Seung Kim, Yong Baek Kim, SungBin Lee, and Myung Joon Han, “Crucial role of out-of-plane sb p orbitals in van hove singularity formation and electronic correlations in the superconducting kagome metal csv_3sb_5 ,” *Phys. Rev. B* **105**, 235145 (2022).
- [62] Rina Tazai, Youichi Yamakawa, Seiichiro Onari, and Hiroshi Kontani, “Mechanism of exotic density-wave and beyond-migdal unconventional superconductivity in kagome metal av_3sb_5 ($a = \text{k, rb, cs}$),” *Science Advances* **8**, eabl4108 (2022).
- [63] Sen Zhou and Ziqiang Wang, “Chern fermi pocket, topological pair density wave, and charge-4e and charge-6e superconductivity in kagomé superconductors,” *Nature Communications* **13**, 7288 (2022).
- [64] Yi-Ming Wu, Ronny Thomale, and S. Raghu, “Sublattice interference promotes pair density wave order in kagome metals,” (2022), [arXiv:2211.01388](https://arxiv.org/abs/2211.01388).
- [65] Haoxiang Li, G. Fabbri, A. H. Said, J. P. Sun, Yu-Xiao Jiang, J.-X. Yin, Yun-Yi Pai, Sangmoon Yoon, Andrew R. Lupini, C. S. Nelson, Q. W. Yin, C. S. Gong, Z. J. Tu, H. C. Lei, J.-G. Cheng, M. Z. Hasan, Ziqiang Wang, Binghai Yan, R. Thomale, H. N. Lee, and H. Miao, “Discovery of conjoined charge density waves in the kagome superconductor csv_3sb_5 ,” *Nature Communications* **13**, 6348 (2022).
- [66] Alexander A. Tsirlin, Pierre Fertey, Brenden R. Ortiz, Berina Klis, Valentino Merkl, Martin Dressel, Stephen D. Wilson, and Ece Uykur, “Role of Sb in the superconducting kagome metal CsV_3Sb_5 revealed by its anisotropic compression,” *SciPost Phys.* **12**, 049 (2022).
- [67] Jonathan Frassinetti, Pietro Bonfà, Giuseppe Allodi, Erick Garcia, Rong Cong, Brenden R. Ortiz, Stephen D. Wilson, Roberto De Renzi, Vesna F. Mitrović, and Samuele Sanna, “Microscopic nature of the charge-density wave in the kagome superconductor rbv_3sb_5 ,” *Phys. Rev. Res.* **5**, L012017 (2023).
- [68] Heqiu Li, Xiaoyu Liu, Yong Baek Kim, and Hae-Young Kee, “Origin of π -shifted three-dimensional charge density waves in the kagomé metal AV_3sb_5 ($a = \text{Cs, Rb, K}$),” *Phys. Rev. B* **108**, 075102 (2023).
- [69] Tian Le, Zhiming Pan, Zhuokai Xu, Jinjin Liu, Jialu Wang, Zhefeng Lou, Zhiwei Wang, Yugui Yao, Congjun Wu, and Xiao Lin, “Evidence for chiral superconductivity in kagome superconductor csv_3sb_5 ,” (2023), [arXiv:2309.00264](https://arxiv.org/abs/2309.00264) [cond-mat.supr-con].
- [70] Maxim Wenzel, Alexander A. Tsirlin, Francesco Capitani, Yuk T. Chan, Brenden R. Ortiz, Stephen D. Wilson, Martin Dressel, and Ece Uykur, “Pressure evolution of electron dynamics in the superconducting kagome metal csv_3sb_5 ,” *npj Quantum Materials* **8**, 45 (2023).
- [71] Harley D Scammell, Julian Ingham, Tommy Li, and Oleg P Sushkov, “Chiral excitonic order from twofold van hove singularities in kagome metals,” *Nature Communications* **14**, 605 (2023).
- [72] Alexander A. Tsirlin, Brenden R. Ortiz, Martin Dressel, Stephen D. Wilson, Stephan Winnerl, and Ece Uykur, “Effect of nonhydrostatic pressure on the superconducting kagome metal csv_3sb_5 ,” *Phys. Rev. B* **107**, 174107 (2023).
- [73] See Supplemental Materials for details on symmetry constraints on the effective Hamiltonian, and the discussion on Ginzburg-Landau analysis.

Supplementary materials

Symmetry constraints on the wave function structure at momentum M

The mirror symmetries m' and m'' perpendicular to the kagome plane put strong constraints on the form of wave function at momentum M . Suppose both vH1 and vH2 are even under m'' and vH1 (vH2) is odd (even) under m' , and the orbital at each kagome site is even (odd) under $m''(m')$ as in Fig.S1(a), where the red (blue) color denotes regions of orbitals with positive (negative) amplitude. This case corresponds to the vHS in AV_3Sb_5 made of d_{xz}, d_{yz} orbitals. Then the wave function components corresponding A,B,C sublattices for vH2 at M_C will take the form $(b, -b, 0)$ as explained in the main text. The explanation for vH1 is as follows. Consider momentum M_C , the wave function of vH1 is odd under m_x and even under m_y , where m_x flips x to $-x$. This leads to the sign structure shown in Fig.S1(a), where the signs denote the region of orbitals with positive/negative amplitude. However, this sign structure is not allowed for a wave function with momentum M_C , because a wave function with momentum M_C should have opposite signs at sites A and A', as seen by $e^{iM_C \cdot (r_A - r_{A'})} = e^{iM_C \cdot (r_B - r_{B'})} = -1$. Therefore the wave function amplitude has to vanish at sublattice A and B. This leads to the form of wave function $(0, 0, b')$ for vH1 at M_C in Fig.1(c) in the main text.

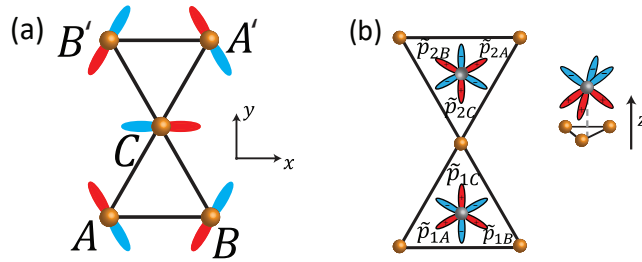


FIG. S1. Illustration of the orbitals used in the tight-binding model.

The above discussion assumes the orbital is even (odd) under $m''(m')$. In the following we show that this assumption can be released such that the conclusion is applicable to orbitals with any symmetries under m' and m'' . Denote $\phi_{m'}$ and $\phi_{m''}$ as the eigenvalues of the orbital under m' and m'' and denote $u_{m'}$ and $u_{m''}$ as the eigenvalues of the wave function at vHS under m' and m'' . $(\phi_{m'}, \phi_{m''}) = (-1, +1)$ corresponds to the orbitals in Fig.S1(a) discussed above. $(\phi_{m'}, \phi_{m''}) = (+1, -1)$ corresponds to the orbitals in Fig.S1(a) rotated by 90 degree. $(\phi_{m'}, \phi_{m''}) = (+1, +1)$ denotes orbitals with s-wave symmetry. $(\phi_{m'}, \phi_{m''}) = (-1, -1)$ denotes orbitals with symmetry of d_{xy} . Since $\phi_{m'}, \phi_{m''}, u_{m'}, u_{m''}$ can be ± 1 independently, it leads to 16 different cases. We enumerate these 16 cases in Fig.S2. We focus on vHS at momentum M_C without loss of generality and write down the allowed form of wave function components at A,B,C sublattices for each case. Each figure shows the orbital orientation consistent with mirror symmetries, where the \pm signs denote the region of orbital with positive/negative amplitude. Some of the symmetry combinations give wave function structure of $(0, 0, 0)$, which means this orbital type cannot give rise to a vHS at momentum M with the given mirror eigenvalues. Take the combination $(\phi_{m'}, \phi_{m''}, u_{m'}, u_{m''}) = (+1, +1, -1, -1)$ for example. The sign structure in Fig.S2 is consistent with the mirror eigenvalues. However, it contradicts with the property of a wave function at momentum M_C which requires that the wave function amplitude should have opposite signs between sites A and A' due to $e^{iM_C \cdot (r_A - r_{A'})} = -1$. Hence this symmetry combination is not allowed.

From Fig.S2 we find that, no matter what symmetry does the orbital has, the wave functions at vH1 and vH2 will take the form of Fig.1(c) as long as the following conditions are satisfied: (1) vH1 and vH2 have opposite eigenvalues for m' and same eigenvalues for m'' . (2) vH1 and vH2 are made of the same orbital type. These conditions result in the wave functions in Fig.1(c), which is crucial for the emergence of loop current order.

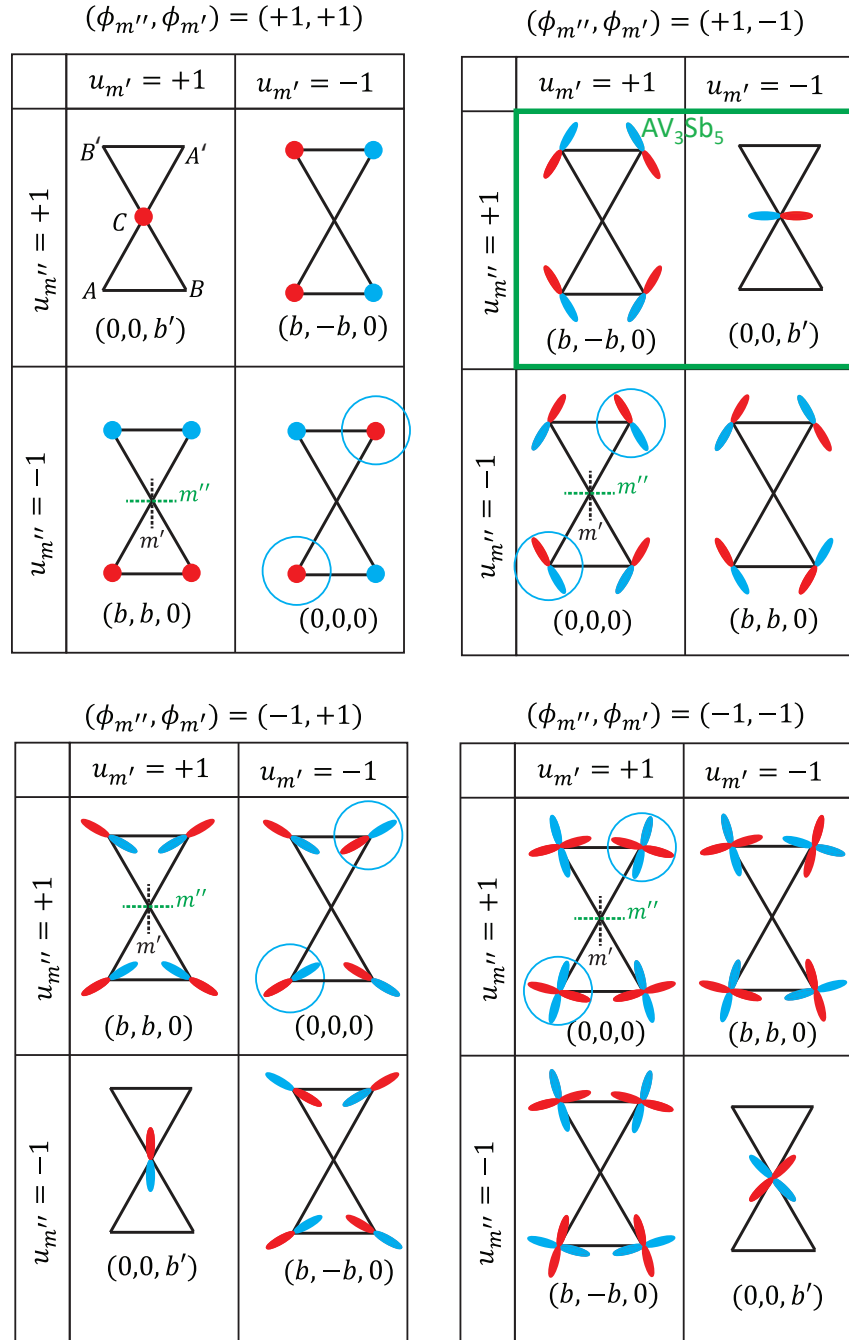


FIG. S2. Orbital arrangement for the wave function of vHS at momentum M_C under different symmetry conditions. The allowed form of wave function components at sublattice A,B,C are shown in the parentheses. The red (blue) color denotes regions of orbitals with positive (negative) amplitude. The wave function amplitude at sites marked by blue circles have the same sign, which contradicts with the requirement of being at momentum M_C and hence it is not allowed. The green box labels the symmetry conditions relevant to AV_3Sb_5 .

Details on derivation of effective model H_{eff}

More details on the derivation of H_{eff} in the main text are given as follows. We start from the Hamiltonian $H(k)$ of the 9-band model [S68], with basis chosen as $\{\tilde{\Phi}\} = \{\tilde{d}_A, \tilde{d}_B, \tilde{d}_C, \tilde{p}_{1A}, \tilde{p}_{1B}, \tilde{p}_{1C}, \tilde{p}_{2A}, \tilde{p}_{2B}, \tilde{p}_{2C}\}$. Here \tilde{d} orbitals are:

$$\begin{aligned}\tilde{d}_A &= -\frac{1}{2}d_{A,xz} + \frac{\sqrt{3}}{2}d_{A,yz} \\ \tilde{d}_B &= -\frac{1}{2}d_{B,xz} - \frac{\sqrt{3}}{2}d_{B,yz} \\ \tilde{d}_C &= d_{C,xz}.\end{aligned}\tag{S1}$$

The orbitals $\tilde{p}_{\sigma\alpha}^-$ with $\sigma = 1, 2$, $\alpha = A, B, C$ are superpositions of p orbitals at the four out-of-plane Sb sites with negative eigenvalue of M_z . $\tilde{p}_{\sigma\alpha}^- \equiv (\tilde{p}_{\sigma\alpha} - M_z \tilde{p}_{\sigma\alpha})/\sqrt{2}$, and $\tilde{p}_{\sigma\alpha}$ is shown in Fig.S1(b) with $\sigma = 1, 2$ representing the two Sb sites above the kagome plane, which are explicitly written as:

$$\begin{aligned}\tilde{p}_{1A} &= -\frac{1}{\sqrt{2}}p_{1x} - \frac{1}{\sqrt{6}}p_{1y} - \frac{1}{\sqrt{3}}p_{1z}, \quad \tilde{p}_{2A} = \frac{1}{\sqrt{2}}p_{2x} + \frac{1}{\sqrt{6}}p_{2y} - \frac{1}{\sqrt{3}}p_{2z}, \\ \tilde{p}_{1B} &= \frac{1}{\sqrt{2}}p_{1x} - \frac{1}{\sqrt{6}}p_{1y} - \frac{1}{\sqrt{3}}p_{1z}, \quad \tilde{p}_{2B} = -\frac{1}{\sqrt{2}}p_{2x} + \frac{1}{\sqrt{6}}p_{2y} - \frac{1}{\sqrt{3}}p_{2z} \\ \tilde{p}_{1C} &= \sqrt{\frac{2}{3}}p_{1y} - \frac{1}{\sqrt{3}}p_{1z}, \quad \tilde{p}_{2C} = -\sqrt{\frac{2}{3}}p_{2y} - \frac{1}{\sqrt{3}}p_{2z}\end{aligned}\tag{S2}$$

The hopping amplitudes and onsite potentials are obtained from DFT, which leads to the 9-band model $H(k)$. We choose the convention of Fourier transform as $c_{k,\rho}^\dagger = \frac{1}{\sqrt{N_c}} \sum_R c_{R,\rho}^\dagger e^{ik \cdot (R+r_\rho)}$, where R labels unit cells, $\rho = 1, \dots, 9$ denotes the orbitals in $\{\tilde{\Phi}\}$ and r_ρ is the location within the unit cell. Then $H(k)$ has a threefold rotation symmetry C_3 given by:

$$C_3 = \begin{pmatrix} 1 & 0 & 0 \\ 0 & 1 & 0 \\ 0 & 0 & 1 \end{pmatrix} \otimes \begin{pmatrix} 0 & 0 & 1 \\ 1 & 0 & 0 \\ 0 & 1 & 0 \end{pmatrix}, \quad C_3 H(k) C_3^\dagger = H(C_3 k)\tag{S3}$$

$H(k)$ can be diagonalized by $U(k)^\dagger H(k) U(k) = \Lambda(k)$ with $\Lambda_{11} \geq \Lambda_{22} \geq \dots \geq \Lambda_{99}$. At momentum M , the energy of vH1 (vH2) is Λ_{44} (Λ_{33}). With CDW orders connecting different M points, the mean field Hamiltonian near the M points is written as

$$H_{MF}(k) = \begin{pmatrix} H(k + M_A) & D^{AB}(k) & D^{CA}(k)^\dagger \\ D^{AB}(k)^\dagger & H(k + M_B) & D^{BC}(k) \\ D^{CA}(k) & D^{BC}(k)^\dagger & H(k + M_C) \end{pmatrix}.\tag{S4}$$

Here k denotes the small deviation from M points, and k is taken to be inside a small hexagon with side length $k_{cut} \ll |G|$, where G is reciprocal lattice vector. $D^{\alpha\beta}$ is a 9×9 matrix from mean field doubling of the interaction. It has nonzero elements only in the first 3×3 diagonal block corresponding to \tilde{d} orbitals, which is denoted as $\overline{D}^{\alpha\beta}$. Consider the threefold symmetric CDW phase with $\Delta_{AB} = \Delta_{BC} = \Delta_{CA} \equiv \Delta$, the explicit forms of $\overline{D}^{\alpha\beta}(k)$ are:

$$\overline{D}^{AB}(k) = -2 \cos \frac{k \cdot d_{AB}}{2} \begin{pmatrix} 0 & \Delta & 0 \\ \Delta^* & 0 & 0 \\ 0 & 0 & 0 \end{pmatrix}, \quad \overline{D}^{BC}(k) = -2 \cos \frac{k \cdot d_{BC}}{2} \begin{pmatrix} 0 & 0 & 0 \\ 0 & 0 & \Delta \\ 0 & \Delta^* & 0 \end{pmatrix}, \quad \overline{D}^{CA}(k) = -2 \cos \frac{k \cdot d_{CA}}{2} \begin{pmatrix} 0 & 0 & \Delta^* \\ 0 & 0 & 0 \\ \Delta & 0 & 0 \end{pmatrix}.\tag{S5}$$

To construct the 6×6 effective Hamiltonian H_{eff} near vH1 and vH2, We perform a unitary transformation to define $\tilde{H}(k) = U^\dagger H_{MF}(k) U$, where U is given by

$$U = \begin{pmatrix} U(M_A) & 0 & 0 \\ 0 & U(M_B) & 0 \\ 0 & 0 & U(M_C) \end{pmatrix}.\tag{S6}$$

It is essential to fix $U(M_B) = C_3 U(M_A)$, $U(M_C) = C_3 U(M_B)$ to eliminate the gauge ambiguity between different M points. The k -independent form of C_3 matrix is important in this gauge fixing procedure. The diagonal elements of $\tilde{H}(k)$ at $k = 0$ represent the energies of the original Hamiltonian at momentum M , which also include vH1 and vH2. To construct an effective

Hamiltonian that describes the vHS, we only keep the columns and rows in $\tilde{H}(k)$ corresponding to vH1 and vH2. More precisely, because vH1 and vH2 are the fourth and the third largest eigenvalues, H_{eff} is a 6×6 matrix obtained from the 3, 4, 12, 13, 21, 22-th columns and rows of $\tilde{H}(k)$. Therefore H_{eff} captures the influence of CDW order on vHS as well as the hybridization between vH1 and vH2 due to the deviation from momentum M . We make a further approximation by keeping only the leading order Taylor expansion of H_{eff} . Let $u_n(k)$ be the 9-component wave function of $H(k)$ at vHn with $n = 1, 2$. By choosing the basis $\{u_1(M_A), u_1(M_B), u_1(M_C), u_2(M_A), u_2(M_B), u_2(M_C)\}$, we get the following form of H_{eff} :

$$H_{\text{eff}}(\mathbf{k}, \Delta) = \begin{pmatrix} \epsilon_1 & s_1\Delta & s_1\Delta^* & \lambda^*k_1 & 0 & 0 \\ s_1\Delta^* & \epsilon_1 & s_1\Delta & 0 & \lambda^*k_2 & 0 \\ s_1\Delta & s_1\Delta^* & \epsilon_1 & 0 & 0 & \lambda^*k_3 \\ \lambda k_1 & 0 & 0 & \epsilon_2 & s_2\Delta^* & s_2\Delta \\ 0 & \lambda k_2 & 0 & s_2\Delta & \epsilon_2 & s_2\Delta^* \\ 0 & 0 & \lambda k_3 & s_2\Delta^* & s_2\Delta & \epsilon_2 \end{pmatrix},$$

$$\equiv \begin{pmatrix} P_1 & Q^\dagger \\ Q & P_2 \end{pmatrix}. \quad (\text{S7})$$

This is the effective Hamiltonian introduced in the main text.

Constraints on the effective Hamiltonian from the sublattice structure of wave functions

The symmetry and the structure of wave functions at vH1 and vH2 in Fig.1(c) in the main text imposes strong constraints on the form of effective Hamiltonian in Eq.(S7). In particular, it enforces the off-diagonal block Q to be a diagonal matrix. This can be seen by explicitly writing down the elements of Q : $Q(k)_{\alpha\beta} = \sum_{ij} u_{1i}(M_\alpha)^* D_{ij}^{\alpha\beta}(k) u_{2j}(M_\beta)$, where $u_{nj}(M_\alpha)$ is the j -th element of $u_n(M_\alpha)$ with $\alpha, \beta = A, B, C = 1, 2, 3$. Then from Fig.1(c) the off-diagonal element of Q vanishes identically because it meets a zero in the wave function at either vH1 or vH2. Explicitly, one can show that:

$$Q_{1,2} = u_1(M_A)^\dagger D^{AB}(0) u_2(M_B) = (b^* \ 0 \ 0) \begin{pmatrix} 0 & -2\Delta & 0 \\ -2\Delta^* & 0 & 0 \\ 0 & 0 & 0 \end{pmatrix} \begin{pmatrix} -b \\ 0 \\ b \end{pmatrix} = b^* \times (-2\Delta) \times 0 = 0 \quad (\text{S8})$$

Here we only wrote down the first three components corresponding to the \tilde{d} orbitals because $D^{\alpha\beta}$ has nonzero elements only at \tilde{d} orbitals. The other off-diagonal elements of Q vanish in a similar way as Eq.(S8). Furthermore, the diagonal elements of Q should vanish when $k = 0$ because ϵ_1 and ϵ_2 are exact eigenvalues at $k = 0$ in the absence of CDW. Therefore, Q is a diagonal matrix with the leading order diagonal elements linear in k . Another important consequence of the sublattice structure of wave function in Fig.1(c) is that the coefficient of the real part of Δ has opposite sign between blocks P_1 and P_2 . This can be seen from the explicit expression $(P_n)(k)_{\alpha\beta} = \sum_{ij} u_{ni}(M_\alpha)^* D_{ij}^{\alpha\beta}(k) u_{nj}(M_\beta)$ for $n = 1, 2$. At momentum M represented by $k = 0$ it gives:

$$(P_1)_{1,2} = u_1(M_A)^\dagger D^{AB}(0) u_1(M_B) = (b^* \ 0 \ 0) \begin{pmatrix} 0 & -2\Delta & 0 \\ -2\Delta^* & 0 & 0 \\ 0 & 0 & 0 \end{pmatrix} \begin{pmatrix} 0 \\ b' \\ 0 \end{pmatrix} = -2|b'|^2 \Delta \equiv s_1 \Delta \quad (\text{S9})$$

$$(P_2)_{1,2} = u_2(M_A)^\dagger D^{AB}(0) u_2(M_B) = (0 \ b^* \ -b^*) \begin{pmatrix} 0 & -2\Delta & 0 \\ -2\Delta^* & 0 & 0 \\ 0 & 0 & 0 \end{pmatrix} \begin{pmatrix} -b \\ 0 \\ b \end{pmatrix} = 2|b|^2 \Delta^* \equiv s_2 \Delta^* \quad (\text{S10})$$

Therefore $s_1 = -2|b'|^2 < 0$ and $s_2 = 2|b|^2 > 0$.

Other types of loop current orders

In the main text we focused on the loop current order with a pattern given in Fig.2(a) denoted as LCBO. There are other possible LCO patterns with the same periodicity, such as the (3,-1,-1,-1) phase [S59] in Fig.S3(a), denoted as LCO'. In LCO' the direction of current is clockwise in one of the hexagons in the extended unit cell and counterclockwise in the other three hexagons, and the magnitude of current in the clockwise hexagon is three times as large as the current in the other hexagons. We demonstrate that LCO' has higher free energy than the LCBO phase considered in the main text, hence LCO' is energetically unfavored.

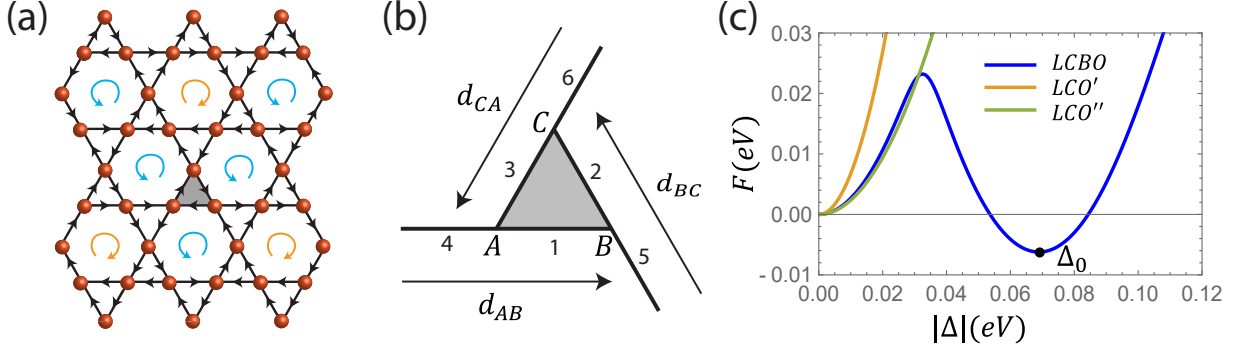


FIG. S3. (a): Illustration of Loop current orders LCO' and LCO''. Each hexagon has either clockwise or counterclockwise currents. For LCO', the currents at the edges of the clockwise hexagons are three times as large as those in counterclockwise hexagons. For LCO'', the current on all bonds have the same magnitude. (b): Notations for distinct bonds in the shaded triangle in (a). (c): Free energy for LCBO, LCO' and LCO'' under the same interaction strength. LCBO is energetically favored as the ground state.

To characterize the order parameter in LCO', we choose the origin inside the shaded upper triangle in Fig.S3(a) and denote the six distinct bonds in the original unit cell by 1~6 as in Fig.S3(b). Let $\Delta_l(R)$ denote the current on the l -th bond ($l = 1 \sim 6$) in unit cell R . Due to the 2×2 periodicity, $\Delta_l(R)$ can be decomposed as $\Delta_l(R) = \sum_Q \Delta_{l,Q} \cos(Q \cdot R)$ where Q is summed over $0, Q_{AB}, Q_{BC}, Q_{CA}$. Different LCO patterns correspond to different choices of $\Delta_{l,Q}$. Denote the current at the edges of counterclockwise hexagons as Δ . The values of $\Delta_{l,Q}$ for LCO' is given by:

	1	2	3	4	5	6
Γ	0	0	0	0	0	0
Q_{AB}	$-\Delta$	Δ	Δ	Δ	$-\Delta$	Δ
Q_{BC}	Δ	$-\Delta$	Δ	Δ	Δ	$-\Delta$
Q_{CA}	Δ	Δ	$-\Delta$	$-\Delta$	Δ	Δ

TABLE I. Values of $\Delta_{l,Q}$ with $l = 1 \sim 6, Q \in \{0, Q_{AB}, Q_{BC}, Q_{CA}\}$ corresponding to LCO'. Γ denotes $Q = 0$.

The contribution from LCO to the Hamiltonian is given by:

$$\hat{H}_\Delta = - \sum_{l=1}^6 \sum_{Q \in \{0, Q_{AB}, Q_{BC}, Q_{CA}\}} \Delta_{l,Q} \hat{O}_{l,Q} + \frac{N_c}{4} \sum_{j=1}^{24} \frac{|\Delta_j|^2}{V} \quad (\text{S11})$$

$$\hat{O}_{1,Q} = \sum_R \left(i c_{R,A}^\dagger c_{R,B} + h.c. \right) \cos(Q \cdot R)$$

$$\hat{O}_{2,Q} = \sum_R \left(i c_{R,B}^\dagger c_{R,C} + h.c. \right) \cos(Q \cdot R)$$

$$\hat{O}_{3,Q} = \sum_R \left(i c_{R,C}^\dagger c_{R,A} + h.c. \right) \cos(Q \cdot R)$$

$$\hat{O}_{4,Q} = \sum_R \left(i c_{R,A}^\dagger c_{R-d_{AB},B} + h.c. \right) \cos(Q \cdot R)$$

$$\hat{O}_{5,Q} = \sum_R \left(i c_{R,B}^\dagger c_{R-d_{BC},C} + h.c. \right) \cos(Q \cdot R)$$

$$\hat{O}_{6,Q} = \sum_R \left(i c_{R,C}^\dagger c_{R-d_{CA},A} + h.c. \right) \cos(Q \cdot R) \quad (\text{S12})$$

Here R is summed over original unit cells, N_c is the number of original unit cells and Δ_j is the current on the 24 distinct bonds in the extended unit cell. For LCO', there are six bonds with $\Delta_j = 3\Delta$ and 18 bonds with $\Delta_j = \Delta$.

The free energy of LCO' can be computed via Eq.(S11) with the coefficients in Table.I. Using the effective Hamiltonian of LCO' with parameters $\epsilon_1 = 6.16eV, \epsilon_2 = 6.4eV, \mu = 6.28eV, V = 0.9eV, T = 7.8meV, b = 0.52, b' = 0.96$, the free energy of LCO' as a function of the magnitude of current $|\Delta|$ is plotted in Fig.S3(c). It shows that LCO' has a much higher free

energy compared to LCBO at the same interaction strength. LCBO has a nonzero global minimum Δ_0 corresponding to Fig.2(a) discussed in the main text, whereas the LCO' only has a trivial minimum at zero. Therefore LCO' is energetically unfavored compared to LCBO.

The large free energy of LCO' mainly comes from the non-uniform distribution of currents, i.e., a bond with current 3Δ contribute a term $9|\Delta|^2/V$ to the free energy, which is nine times as large as a bond with current Δ . We can also consider another pattern of loop current order in which the direction of currents in each bond is the same as LCO' but all the bonds have the same magnitude of current. Denote this phase as LCO'' and let the current on each bond be $\pm\Delta$. The values of $\Delta_{l,Q}$ for LCO'' is given by:

	1	2	3	4	5	6
Γ	$\frac{\Delta}{2}$	$\frac{\Delta}{2}$	$\frac{\Delta}{2}$	$\frac{\Delta}{2}$	$\frac{\Delta}{2}$	$\frac{\Delta}{2}$
Q_{AB}	$-\frac{\Delta}{2}$	$\frac{\Delta}{2}$	$\frac{\Delta}{2}$	$\frac{\Delta}{2}$	$-\frac{\Delta}{2}$	$\frac{\Delta}{2}$
Q_{BC}	$\frac{\Delta}{2}$	$-\frac{\Delta}{2}$	$\frac{\Delta}{2}$	$\frac{\Delta}{2}$	$\frac{\Delta}{2}$	$-\frac{\Delta}{2}$
Q_{CA}	$\frac{\Delta}{2}$	$\frac{\Delta}{2}$	$-\frac{\Delta}{2}$	$-\frac{\Delta}{2}$	$\frac{\Delta}{2}$	$\frac{\Delta}{2}$

TABLE II. Values of $\Delta_{l,Q}$ with $l = 1 \sim 6$, $Q \in \{0, Q_{AB}, Q_{BC}, Q_{CA}\}$ corresponding to LCO''. Γ denotes $Q = 0$.

The free energy of LCO'' is also plotted in Fig.S3(c). It is higher than LCBO, and it only has a trivial minimum at zero. Therefore the energetically favored phase is LCBO.

Ginzburg-Landau analysis and the effect of dispersion near vHS

Many studies computed the CDW phase diagram via a Ginzburg-Landau (GL) approach by expanding the free energy as a power series of order parameter Δ . Since the GL approach is a perturbation method for small Δ near the Fermi surface, the phase diagram obtained by the GL method is sensitive to the dispersion near the vHS. In the following, we will show that the CDW order we found is beyond the perturbation theory for small Δ , hence it cannot be described by GL free energy and is not sensitive to the dispersion near the vHS.

The free energy of the system described by H_{eff} is given by:

$$F(\Delta) = -\frac{1}{N}T \sum_{n,\mathbf{k}} \text{Tr} \log[-G_{n,\mathbf{k}}^{-1}(\Delta)] + \frac{6|\Delta|^2}{V}, \quad (\text{S13})$$

where $G_{n,\mathbf{k}}(\Delta) = \frac{1}{i\omega_n - H_{\text{eff}}(\mathbf{k},\Delta) + \mu}$ and the factor of 6 comes from the six bonds in each original unit cell. The GL free energy $F_{GL}(\Delta)$ is obtained by expanding the free energy to powers of Δ . The most straightforward way to demonstrate the inability of F_{GL} to capture our CDW solution is by considering the $\lambda = 0$ limit. In this case, the free energy in the complex Δ plane has degenerate minima at $\Delta = -|\Delta|$ and $\Delta = |\Delta|e^{\pm\frac{\pi}{3}i}$ corresponding to CBO and LCBO respectively, where $|\Delta|$ is determined by interaction strength. At these free energy minima, the eigenvalues of $H_{\text{eff}} - \mu$ can be written down analytically by

$$\begin{aligned} E_1 &= \epsilon_2 - \mu - 4|b|^2|\Delta|, & E_2 &= E_3 = \epsilon_1 - \mu - 2|b'|^2|\Delta|, \\ E_4 &= E_5 = \epsilon_2 - \mu + 2|b|^2|\Delta|, & E_6 &= \epsilon_1 - \mu + 4|b'|^2|\Delta|. \end{aligned} \quad (\text{S14})$$

The free energy is given by

$$F(\Delta) = -\frac{1}{4}T \sum_{n=1}^6 \log\left(1 + e^{-\frac{E_n}{T}}\right) + \frac{6|\Delta|^2}{V}, \quad (\text{S15})$$

and the GL free energy F_{GL} is the Taylor expansion of Eq.(S15). We fix the complex phase of Δ to be $\frac{\pi}{3}$ and plot the exact and GL free energy as a function of Δ in Fig.S4(a) with parameters $\epsilon_1 = 6.16eV$, $\epsilon_2 = 6.4eV$, $\mu = 6.28eV$, $V = 0.9eV$, $T = 7.8meV$, $b = 0.52$, $b' = 0.96$, where we have kept $O(|\Delta|^4)$ terms in F_{GL} . The global minimum Δ_0 corresponds to our CDW solution. Fig.S4(a) shows that F and F_{GL} agree with each other when $|\Delta|$ is small, but the global minimum Δ_0 does not appear in F_{GL} . We also find that the coefficients of $O(|\Delta|^6)$, $O(|\Delta|^8)$, ..., $O(|\Delta|^{20})$ terms in F_{GL} are all negative, hence even if we add higher power terms of $|\Delta|$ into F_{GL} , the global minimum at Δ_0 will not show up either. Therefore, the LCBO phase we found cannot be described by GL free energy which is valid only at small $|\Delta|$.

We can estimate the magnitude of Δ required to realize LCBO. From Eq.(4) in the main text, the ground state is LCBO when $4(|b|^2 + |b'|^2)|\Delta| > \epsilon_2 - \epsilon_1$, which implies $|\Delta| > \frac{\epsilon_2 - \epsilon_1}{4(|b|^2 + |b'|^2)} \sim (\epsilon_2 - \epsilon_1)/4 \sim 60meV$. This value is comparable with the magnitude of CDW order parameter $|\Delta| \sim 60meV$ observed in optical conductivity experiments [S21, S28].

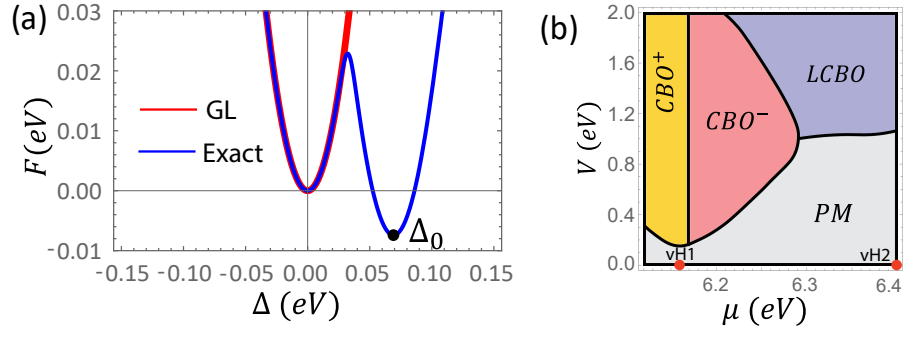


FIG. S4. (a): Comparison between the exact free energy and GL free energy at $\lambda = 0$ with the complex phase of Δ fixed at $\frac{\pi}{3}$. (b): Phase diagram of $H_{\text{eff}} + \delta H$. The other parameters are the same as Fig.4(a) in the main text.

The finite magnitude of Δ makes the CDW phases less sensitive to the detailed dispersion near the vHS. To demonstrate this, we add to the effective Hamiltonian the following saddle-type term obtained from the dispersion of the tight-binding model:

$$\delta H(\mathbf{k}) = \text{diag}\{ g_1(C_3\mathbf{k}), g_1(C_3^{-1}\mathbf{k}), g_1(\mathbf{k}), g_2(C_3\mathbf{k}), g_2(C_3^{-1}\mathbf{k}), g_2(\mathbf{k}) \}, \quad (\text{S16})$$

$$g_1(\mathbf{k}) = -c_1 k_x^2 + c_2 k_y^2, \quad g_2(\mathbf{k}) = c_3 k_x^2 - c_4 k_y^2 \quad (\text{S17})$$

$$(c_1, c_2, c_3, c_4) = (0.46, 1.19, 0.5, 0.39) \text{ eV} \cdot a^2 \quad (\text{S18})$$

Here a is the lattice constant, diag denotes diagonal matrix and C_3 is threefold rotation. The new phase diagram obtained by $H_{\text{eff}} + \delta H$ is shown in Fig.S4(b). It demonstrates that the addition of dispersion near the vHS only results in a slight shift of phase boundaries, but no significant change occurs.